Eur. Phys. J. E **9**, 477–485 (2002)
DOI 10.1140/epje/i2002-10107-0

THE EUROPEAN PHYSICAL JOURNAL E

Numerical study of the flow around a cylinder using multi-particle collision dynamics

A. Lamura[1,2,a] and G. Gompper[1,b]

[1] Institut für Festkörperforschung, Forschungszentrum Jülich, D-52425 Jülich, Germany
[2] Istituto Applicazioni Calcolo, CNR, Sezione di Bari, via Amendola 122/I, 70126 Bari, Italy

Received 23 July 2002 and Received in final form 12 January 2003 /
Published online: 4 February 2003 –

Abstract. A novel mesoscopic simulation technique —multi-particle collision dynamics— which has been suggested very recently, is used to study the two-dimensional flow around a square and a circular cylinder. The method is described and new proper boundary conditions are proposed to deal with wall collisions. The flow is analyzed in a wide range of Reynolds numbers in order to cover both the steady and unsteady regimes, resulting in symmetric steady vortices and periodic vortex shedding, respectively. The numerical results for integral flow parameters, such as the recirculation length, the drag and lift coefficients, the Strouhal number, as well as the spatial dependence of the velocity field, are compared with previous numerical and experimental studies. The qualitative and quantitative agreement is very good, validating the method as a promising technique to describe the hydrodynamic effects of solvent on embedded particles.

PACS. 02.70.Ns Molecular dynamics and particle methods – 47.11.+j Computational methods in fluid dynamics – 82.20.Wt Computational modeling; simulation

1 Introduction

A growing effort in developing novel approaches to simulate the hydrodynamic behavior of complex fluids can be observed in recent years. Several methods have been proposed as interesting alternatives to the classical approaches in computational fluid dynamics, *i.e.*, finite-volume methods for the solution of the Navier-Stokes equation [1,2]. These approaches, such as lattice gas automata (LGA) [3], lattice-Boltzmann methods (LBM) [4–6], and dissipative-particle dynamics (DPD) [7,8], describe fluids at mesoscopic length scales. This means that all the microscopic (molecular) details are omitted and only those features necessary to mimic correctly the hydrodynamic behavior are retained. This has two major advantages: on the one hand, models can be implemented by relatively simple numerical codes; on the other hand, space and time scales are accessible up to the macroscopic level. Each of the aforementioned methods has its own characteristics. LGA and LBM are conceptually simple. However, LGA suffers mainly from the lack of Galilean invariance, and the underlying lattice structure requires the use of adapted computational meshes in the case of complex geometries, while LBM cannot model fluctuating hydrodynamics due to the absence of thermal fluctuations. DPD is immune from these limitations, being an off-lattice method, but the analytical investigation of its properties is often difficult and complex.

In this paper we consider and analyze in detail a new particle-based method suggested very recently by Malevantes and Kapral [9], which shows its potential also in the case of a classical fluid-dynamics problem. The present method, which we will refer to as multi-particle collision dynamics (MPCD) [9,10], is a simplified version of Bird's Direct Simulation Monte Carlo algorithm [11]. The method has also been called stochastic rotation dynamics [12] and Malevantes-Kapral method [13]. The fluid is modeled in terms of particles, which do not correspond to individual molecules but sets of them. Their positions and velocities are continuous variables which are updated at consecutive time steps according to propagation and collision rules. The propagation determines the streaming of each individual particle by its displacement during a finite time interval. The system is partitioned into the cells of a regular lattice with no constraint on the number of particles per cell. Each cell becomes the collision volume for those particles in that cell at that time. A very simple rule for implementing collisions was introduced by Malevanets and Kapral [9]. This rule exactly conserves mass, momentum and energy. An H-theorem holds for this dynamics and the correct hydrodynamic equations are recovered for an ideal gas [9]. A successive work has critically examined

[a] e-mail: a.lamura@area.ba.cnr.it
[b] e-mail: g.gompper@fz-juelich.de

this model pointing out that the collision rule has to be modified at low temperatures in order to correctly restore Galilean invariance [12].

In this paper we present a detailed quantitative analysis for the flow of a two-dimensional incompressible fluid with a parabolic velocity profile in a channel against a square and a circular cylinder. This problem has been extensively studied experimentally for a circular [14–18] and a square cylinder [19,20] and numerically using different approaches, among them mesoscopic methods LBM [21–23], LGA [24–27] (circular cylinder) and LBM [28,29] (square cylinder). The abundance of experimental and numerical results for this problem allows us to carry out extensive benchmarking for this new model. The accordance with available data in the literature is very good and enables us to validate the method. The MPCD method, for which preliminary results have been recently published [10], allows to cover a wide range of Reynolds numbers. Depending on the Reynolds number Re, different flow regimes can be distinguished. At very small Reynolds numbers, no separation takes place at the surface of the cylinder. With increasing Re, the flow separates at the trailing edges of the cylinder and a closed steady recirculation region consisting of two symmetric vortices is observed behind the obstacle. The size of the recirculation region increases linearly with Re. When a critical value Re_c is reached, which is approximately 49 for the circular cylinder [30] and 60 for the square cylinder [29], the well-known von Karman vortex street with periodic vortex shedding from the cylinder can be observed in the wake.

The paper is organized as follows. Section 2 describes in detail the model showing a possible choice for boundary conditions in order to deal with solid boundary walls. Numerical results will be presented in the Section 3, which are discussed and compared with available experimental and numerical studies. The relevant quantities, such as the recirculation length, the drag and lift coefficients and the Strouhal number, are calculated. Moreover, an accurate analysis is performed for the velocity profiles in the case of the square cylinder in order to compare them with the corresponding profiles obtained using LBM in reference [29]. Finally, we draw our conclusions describing possible future applications.

2 The model

In this section we outline the numerical scheme and describe new appropriate no-slip boundary conditions.

2.1 The numerical scheme

We consider a two-dimensional system made of N identical particles of mass m whose positions $\mathbf{r}_i(t)$ and velocities $\mathbf{v}_i(t)$, $i = 1, 2, ..., N$, are continuous variables. The time is discretized in time intervals Δt. The evolution occurs in two consecutive steps: propagation and collision. The propagation of particles is performed by streaming them according to the rule

$$\mathbf{r}_i(t + \Delta t) = \mathbf{r}_i(t) + \mathbf{v}_i(t)\Delta t\,. \tag{1}$$

For the collision step the system is divided into the cells of a regular lattice of mesh size a_0. Each of these cells is the interaction volume where a multi-particle instantaneous collision occurs, which changes particles velocities [9]

$$\mathbf{v}_i(t + \Delta t) = \mathbf{u}(t) + \Omega[\mathbf{v}_i(t) - \mathbf{u}(t)], \tag{2}$$

where $\mathbf{u} = \sum_{i=1}^{n_c} \mathbf{v}_i/n_c$ is the average velocity of the colliding particles, n_c being the number of particles in the cell. The velocity $\mathbf{u}$ is considered to be the macroscopic velocity of the fluid and it is assumed to have the coordinates of the center of the cell. Ω denotes a stochastic rotation matrix which rotates, with equal probability, by angle of either $+\pi/2$ or $-\pi/2$. The collisions are simultaneously performed on all the particles in a cell with the same rotation Ω, but Ω may differ from cell to cell. The local momentum and kinetic energy do not change under this dynamics. The kinetic energy of particles fixes the temperature k_BT, where k_B is the Boltzmann constant, *via* the energy equipartition theorem.

The mean free path $l = \Delta t(k_BT/m)^{1/2}$ plays an important role in establishing the behavior of the system under Galilean transformations. Indeed, as long as l is comparable to or larger than the cell size a_0, a given particle will collide at consecutive times in different cells. On the other hand, when $l < a_0$ (at low temperatures) effects due to correlations between particles, which stay in the cell for several collisions, are changed by the presence of flow. This breaks the Galilean invariance. A way to cure this pathology was introduced in reference [12]. There the following rule was adopted: The lattice is shifted at each time step, before the collision, by a random vector with components in the interval $[-a_0/2, a_0/2]$. This makes the collision volume no more dependent on the macroscopic velocity and Galilean invariance is restored. It is worthwhile at this point to emphasize that, in any case, the MPCD method is most efficient when the cell size is comparable with the mean free path. Indeed, a cell size bigger than the mean free path is not advantageous since spatial resolution is related to the cell size. This case may still be interesting to consider for systems with a large diffusivity. On the other hand, since the hydrodynamic interaction is effective at length scales of several mean free paths, the situation with mean free path larger than the cell size would again require quite big systems to achieve the same spatial resolution.

2.2 Boundary conditions

The new collision rule introduces a problem when solid walls delimit the geometry of the system under consideration. When walls coincide exactly with the boundaries of collision cells, the usual bounce-back rule, which consists in inverting the velocities of particles hitting the walls, is adopted. A different situation occurs when cells are partially filled. This may happen in two different situations:

complex geometries and cell-shifting. In both cases having a fixed lattice size, the boundary cells do not necessarily coincide with the solid walls. In such situations the number n of colliding particles is less than the initial average number $n_{\rm av}$ of particles per cell. We found that a proficient way to perform collisions in the boundary cells is to fill these cells by adding $(n_{\rm av}-n)$ virtual particles [10]. These particles have velocities drawn from a Maxwell-Boltzmann distribution of zero average velocity and the same temperature $k_{\rm B}T$ of the fluid. This enables us to perform collisions, as prescribed by equation (2), within a total number $n_{\rm av}$ of real and virtual particles. In order to save computing time, we note that instead of having $(n_{av}-n)$ independent Gaussian numbers with zero average and fixed variance $k_{\rm B}T/m$, we can consider just a single Gaussian number with zero average and variance $(n_{\rm av}-n)k_{\rm B}T/m$. This means that the average velocity in the boundary cells, to insert in equation (2), will be computed as

$$\mathbf{u} = \frac{\sum_{i=1}^{n} \mathbf{v}_i + \mathbf{a}}{n_{\rm av}}\,, \tag{3}$$

where $\mathbf{a}$ is a vector whose components are numbers taken from a Gaussian distribution with zero average and variance $(n_{\rm av}-n)k_{\rm B}T/m$. Such a rule has been implemented for a Poiseuille flow in a two-dimensional channel for two different cases: low temperature with cell-shifting ($l < a_0$) and fixed-cells lattice ($l \simeq a_0$) displaced with respect to the walls so that the cells fill the channel asymmetrically. In both the cases we looked at both the parabolic velocity profile across the channel to measure the kinematic viscosity and the density profile in order to check anomalous compressibility effects close to the walls. Results are in agreement with other measurements of the kinematic viscosity for the same system and density profile is constant across the channel [10]. This is at odds with what is observed using the collision rule (2) and resting virtual particles, *i.e.* with $\mathbf{a} = 0$ in equation (3). The latter case corresponds to having wall particles at zero temperature (different from our choice to fill cells with particles having the same temperature as the fluid) and leads to a dramatic increase of the density near the walls. Due to these results the modified collision rule will be adopted in the following whenever partly filled lattice cells occur.

3 Numerical results

3.1 The geometry of the system

In the following we will use $m = 1$, $\Delta t = 1$, $a_0 = 1$ and all the lengths will be expressed in terms of the cell size a_0. The system is a two-dimensional rectangular channel with length L and width H. The obstacle is represented by a square and a circular cylinder with diameter D. The center of the cylinder is placed at a distance $L/4$ from the edge of the channel and at a distance $H/2$ from the lateral walls. The geometry is depicted in Figure 1. A x-y reference system is introduced with the origin in the center of the cylinder and the x-axis is directed along the channel. All the lengths will refer to this coordinate system.

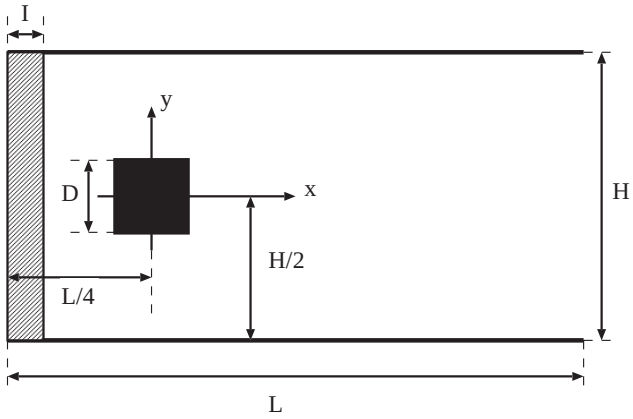

Fig. 1. Definition of the geometry of the simulation box.

The blockage ratio $B = D/H$ is fixed at 0.125, while the ratio L/D is set to 50 in order to reduce the influence of inflow and outflow boundary conditions. The usual periodic boundary conditions are used in the x-direction and no-slip boundary conditions are enforced at the top and the bottom of the channel and at the cylinder walls. The flow is directed along the length of the channel and is driven by assigning to particles in the inflow region I, with a width of 10 lattice cells, Maxwell-Boltzmann–distributed velocities with average value $v_x(y) = 4v_{\rm max}(H-y)y/H^2$ in the x-direction and zero average in the y-direction, so that a steady parabolic velocity profile is maintained in the inflow region. The value of the maximum velocity $v_{\rm max}$ is constrained in order to reduce compressibility effects. Simulations have been carried out for several values of $v_{\rm max}$. For high Reynolds numbers the lowest value used is $v_{\rm max} = 0.2a_0/\Delta t$. This corresponds to a Mach number $M = v_{\rm max}/c_{\rm s}$ which is about 1/4, where $c_{\rm s}$ is the speed of sound which can be computed as $c_{\rm s}^2 = (C_p/C_V){\rm d}p/{\rm d}\rho = 2k_{\rm B}T/m$. Smaller values of $v_{\rm max}$ would have required systems of very large dimensions to reach high values of the Reynolds number. As a matter of fact, the case with $Re = 130$ required the use of a system with $D = 64a_0$ and more than 16 million particles. The temperature will be fixed at $k_{\rm B}T = 0.4m(a_0/\Delta t)^2$. For this choice the mean free path is $l = 0.63a_0$. The initial average density is $n_{\rm av} = 10$. The corresponding kinematic viscosity is $\nu = (0.110 \pm 0.004)a_0^2/\Delta t$.

3.2 Steady flow

Our discussion will be focused on the case of the square cylinder for two reasons: the qualitative behavior is the same for the two types of cylinder, and for the square cylinder we can directly compare our results with previous numerical studies based on LBM and finite-volume method [29], where the same set-up is used. As long as the Reynolds number, $Re = v_{\rm max}D/\nu$, stays smaller than a critical value, which is estimated to be approximately 49

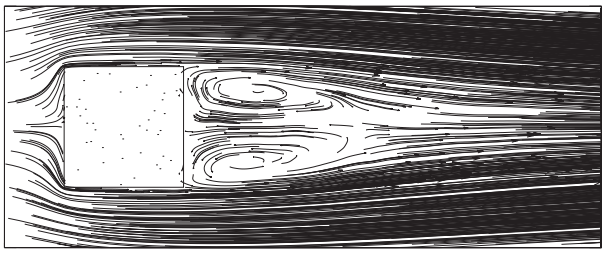

Fig. 2. Velocity field at the final steady state for $Re = 30$. Only a fraction of the simulation box is shown.

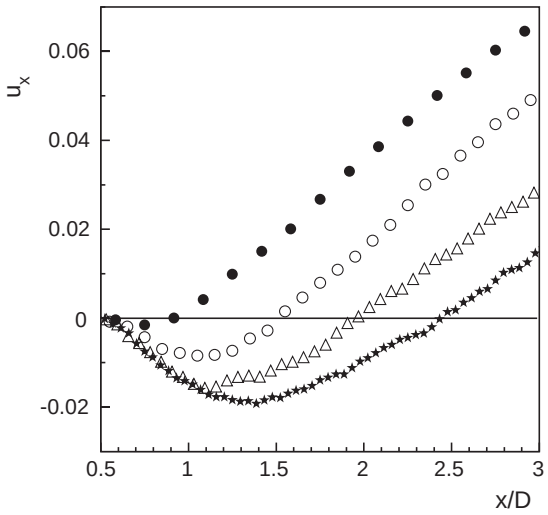

Fig. 3. Velocity distribution of the x-component on the center line ($y/D = 0$) behind the square cylinder at the final steady state for different Re values: $Re = 10$ (•), 20 (○), 30 (△), 40 (⋆). u_x is measured in units of $a_0/\Delta t$.

for the circular cylinder [30] and 60 for the square cylinder [29], a pair of stationary recirculating eddies develops behind the cylinder. Numerical simulations are carried out for four values of Re, 10, 20 , 30, and 40. Flow patterns are consistent with experiments (see Fig. 4 of Ref. [15] for the circular cylinder) and numerical simulations (see Fig. 2 of Ref. [29]). In Figure 2 the streamlines for the steady flow are shown for $Re = 30$. The flow patterns can be characterized in terms of some integral flow parameters. One of these is the recirculation length L_r, which is defined as the distance from the rearmost point of the cylinder to the end of the wake. The presence of the closed wake is revealed by the existence of negative velocities in the axial velocity distribution. Figure 3 shows the time evolution of such a distribution for the x-component of the macroscopic velocity for different values of Re. In the wake, near the axis, the flow direction is opposite to the general one and the recirculation length appears clearly. It is possible to study the evolution of L_r in time. This is shown in Figure 4 for some values of the Reynolds number. The evolution shows an interesting feature below a certain value of Re: The recirculation length passes through a maximum value, at which time the closed wake is more spread out than it is when fully established. This phenomenon which appears clearly for $Re = 20$ is probably caused by a wall effect.

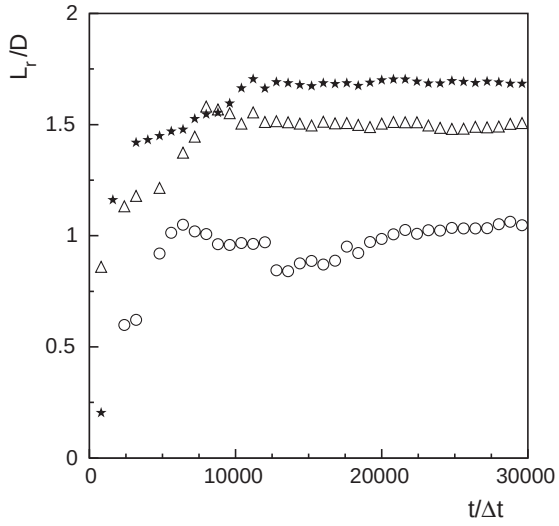

Fig. 4. Evolution with time of the square cylinder recirculation length for different Re values: $Re = 20$ (○), 30 (△), 40 (⋆).

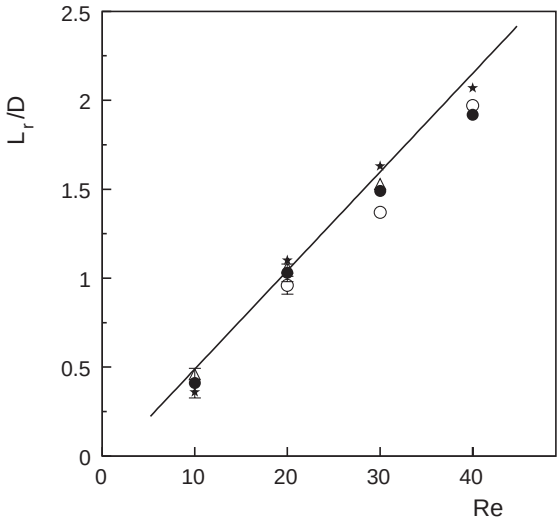

Fig. 5. The recirculation length as a function of the Reynolds number for the square cylinder for different v_max values: this study with $v_\mathrm{max}\Delta t/a_0 = 0.1$ (△), 0.2 (•), 0.3 (⋆) and fixed-cell lattice, this study with $v_\mathrm{max}\Delta t/a_0 = 0.2$ (○) and cell-shifting; (——) Breuer *et al.* [29].

Indeed in reference [15] it is shown that the greater is the value of the blockage ratio B, the more significant is the phenomenon. In this paper we focus on the dependence of results on the velocity v_max keeping B fixed. Apart from this wall effect, it appears that the curves for L_r tend towards their steady-state value more quickly for small Re. In Figure 5 L_r is reported as a function of Re. The figure also shows the dependence of L_r on the inflow velocity v_max for fixed Reynolds number. In the latter case, L_r does not have a monotonic dependence on v_max. However, it appears that L_r grows linearly with Re for all the values of v_max. The values of L_r/D are affected by errors which are estimated to be $a_0/(2D)$. The reason is due to the fact that the position of the macroscopic velocity $\mathbf{u}$ in each

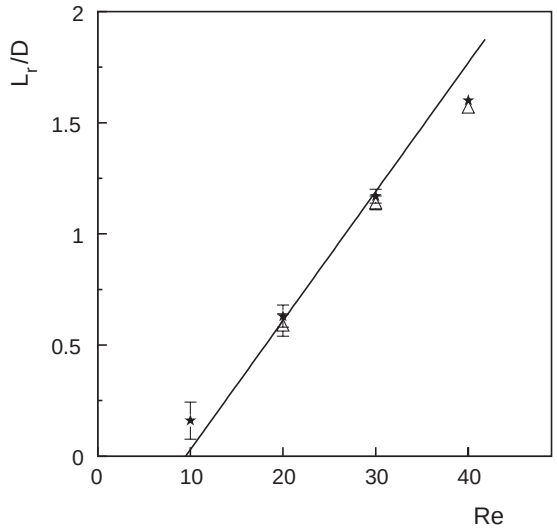

Fig. 6. The recirculation length for the circular cylinder as a function of the Reynolds number: this study at $v_{\max}\Delta t/a_0 = 0.2$ with fixed-cell lattice ($\star$), and cell-shifting ($\triangle$); (——) Coutanceau and Bouard [15].

cell is arbitrarily taken to be the center of the cell. For $v_{\max} = 0.2a_0/\Delta t$ we considered the cases with fixed-cell lattice and cell-shifting (the cell-shifting was not considered at $Re = 10$ because the error bars are much larger than the difference between the two simulation methods anyway). In both the cases a linear fit to our data gives

$$\frac{L_{\rm r}}{D} = mRe + q \tag{4}$$

with $m = 0.0525 \pm 0.0020$ and $q = 0.148 \pm 0.069$. In reference [29], where the simulated system has the same blockage ratio and inflow conditions using LBM and finite-volume methods, it is found $m = 0.0554$ and $q = 0.065$. The slopes are very similar, but our values are slightly shifted to lower values. No experimental data could be found in the literature for the same blockage ratio. Indeed, the quantity $L_{\rm r}$ is a sensitive function on B, and it increases with decreasing B [15]. The numerical results for the circular cylinder are shown in Figure 6, where they are compared with the only available experimental results for a similar value of the blockage ratio ($B = 0.12$) [15].

Another important flow parameter is the drag coefficient defined by

$$C_{\rm d} = \frac{2F_x}{n_{\rm av}v_{\max}^2 D}\,, \tag{5}$$

where F_x is the force exerted on the cylinder in the x-direction. The plot of $C_{\rm d}$ as function of Re will be shown in the next section over the whole range of the considered value of the Reynolds number.

3.3 Unsteady flow

Beyond the aforementioned critical value $Re_{\rm c}$, the von Karman vortex street is observed and a periodic vortex shedding is produced in the rear of the cylinder. We studied the flow for Reynolds numbers up to 130. A characteristic flow pattern for such a situation is shown in Figure 7 for $Re = 100$. Each picture was obtained by averaging over four consecutive velocity patterns separated by one period. Four such averaged velocity patterns, equally spaced in the time of one period, elucidate the periodic nature of the phenomenon. One can see a small vortex developing at the rear bottom edge of the cylinder, which moves upwards while growing, and then leaves the edge of the obstacle. The next vortex starts at the rear top edge, moves downwards and grows to separate finally from the top edge.

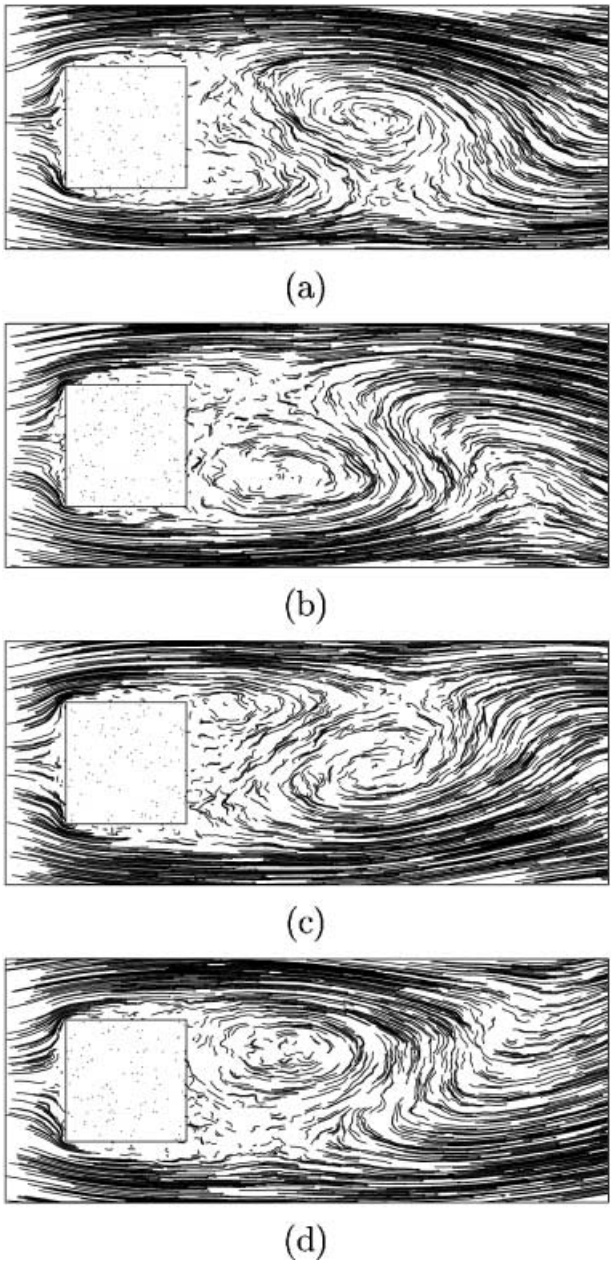

Fig. 7. Velocity field at consecutive (from (a) to (d)) equally spaced times in one period of vortex shedding for $Re = 100$. Only a fraction of the simulation box is shown.

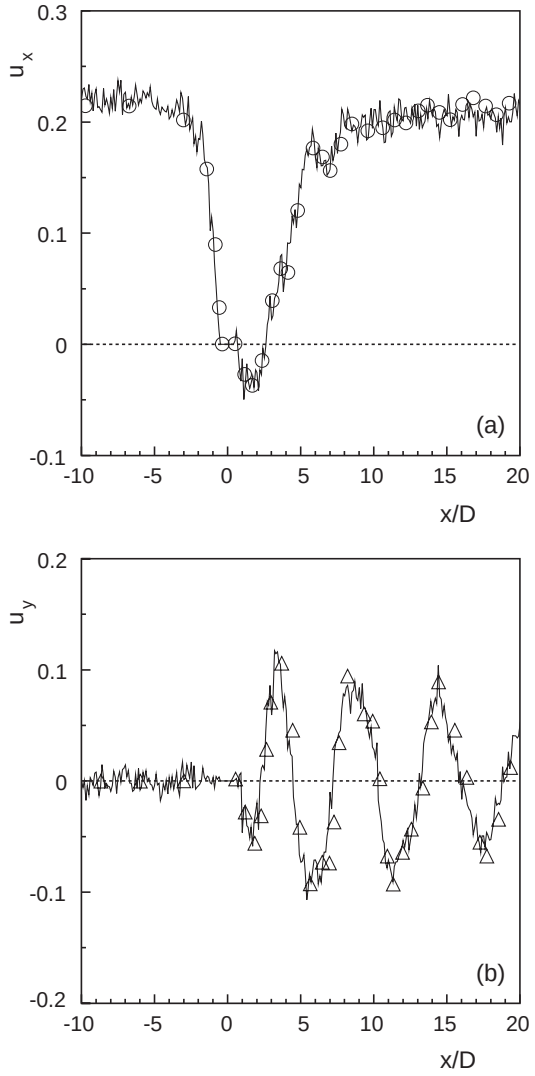

Fig. 8. Velocity distributions of (a) the x and (b) the y components along the centerline ($y/D = 0$) at a certain moment (see the text for explanation) for the square cylinder at $Re = 100$. For a comparison, LBM data from Breuer *et al.* [29] are also shown: x-component (○) and y-component (△). u_x and u_y are measured in units of $a_0/\Delta t$.

In order to study the velocity profiles, we need to define the moment of evaluation since the flow is unsteady. We choose the time at which the velocity u_y changes its sign from plus to minus with a linearly decreasing profile in the x-range $10.4D$–$10.6D$ along the centerline $y/D = 0$. The time series is divided into subsequent sets of 80 iterations each and individual velocity profiles are averaged over these iteration sets before every evaluation to reduce the noise. Profiles shown in Figure 8 have been obtained by averaging in addition over eight of such profiles (calculated at different cycles of vortex shedding) to smooth out the individual noisy signals. The relative error for each velocity value is then about 10%. This error is comparable with the noise of the velocity profiles in Figures 8, 9. At the same times, velocity profiles across the channel were also

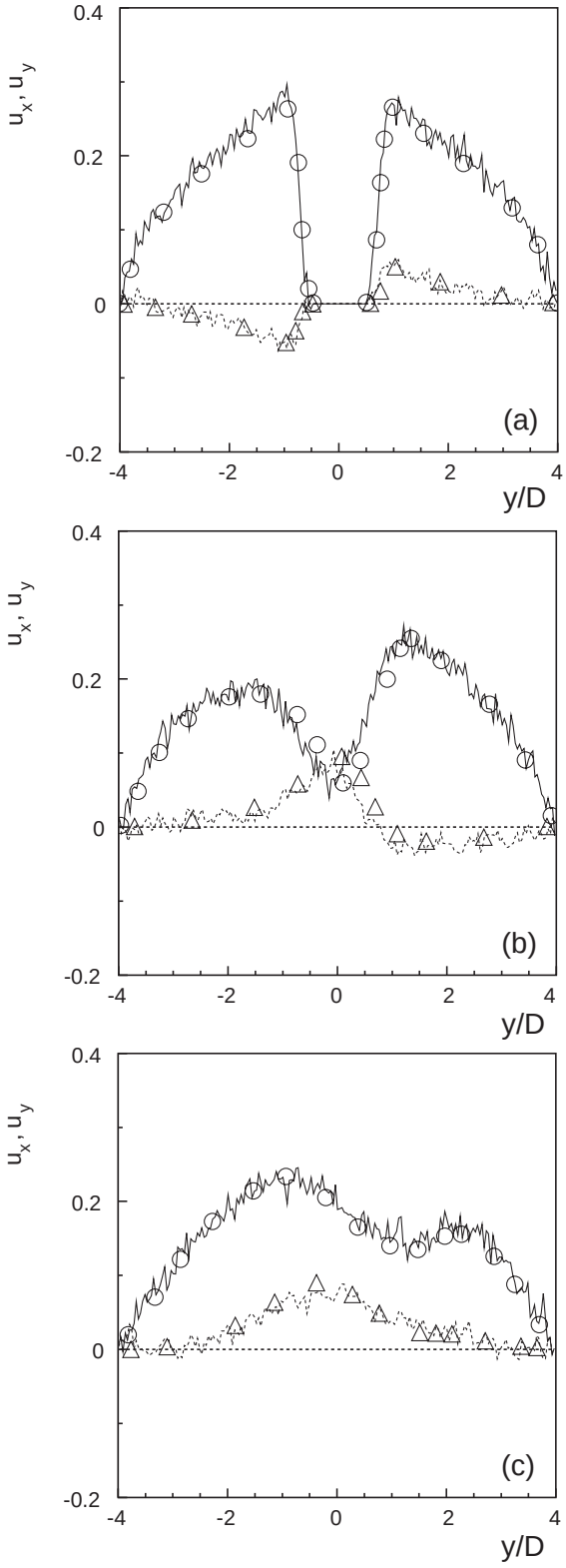

Fig. 9. Velocity distributions of the x (full line) and y (dashed line) components across the channel at a certain moment (see the text for explanation) at three different positions: (a) $x/D = 0$, (b) $x/D = 4$, (c) $x/D = 8$ for the square cylinder at $Re = 100$. For a comparison, numerical LBM data from Breuer *et al.* [29] are also shown: x-component (○) and y-component (△). u_x and u_y are measured in units of $a_0/\Delta t$.

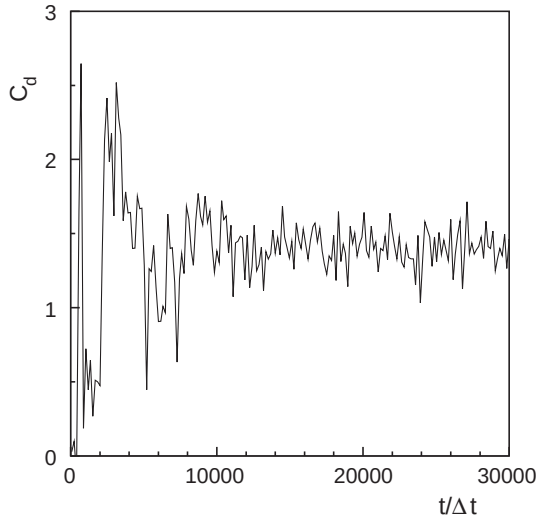

Fig. 10. Time evolution of the drag coefficient for the square cylinder at $Re = 100$.

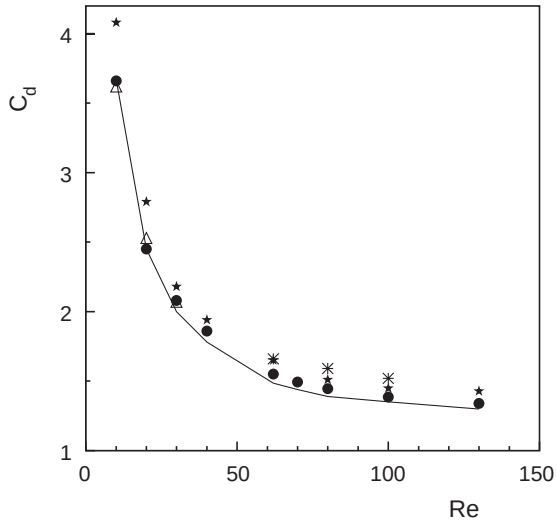

Fig. 11. The drag coefficient for the square cylinder as a function of the Reynolds number for different $v_{\max}$ values: this study with $v_{\max}\Delta t/a_0 = 0.1$ (△), 0.2 (•), 0.3 (⋆), 0.36 (∗); (——) Breuer *et al.* [29].

considered and are shown in Figure 9 at three different positions $x/D = 0, 4, 8$. The velocity profiles of Figures 8, 9 are compared with the corresponding ones obtained using the same parameters and inflow conditions with LBM in reference [29]. Apart from the fluctuations which characterize our data, the qualitative and quantitative agreement is very good, and also profile details are reproduced by our method. The drag coefficient $C_{\rm d}$ is computed and its time evolution for $Re = 100$ is shown in Figure 10. After an initial transient, $C_{\rm d}$ gradually evolves to periodic oscillations. The computed value of the drag coefficient is given by a time average over the time range when the periodic vortex shedding has been established. $C_{\rm d}$ as a function of Re is reported in Figure 11 where also the dependency on $v_{\max}$ is investigated. The continuous line represents the value

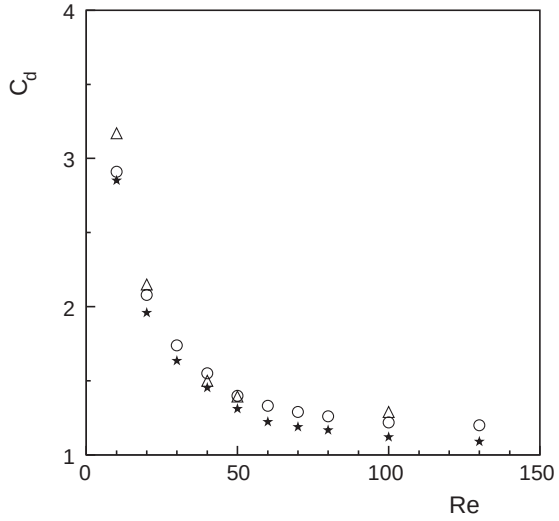

Fig. 12. The drag coefficient for the circular cylinder as a function of the Reynolds number: this study (⋆) with $v_{\max}\Delta t/a_0 = 0.2$, (○) Tritton [14], (△) He and Doolen [23].

obtained using LBM [29]. It can be clearly seen that a significant improvement in the agreement is achieved by diminishing $v_{\max}$, even if a small but systematic deviation to larger values compared to reference [29] remains. No data were found in the literature for experiments with the same value of the blockage ratio. In the case of the circular cylinder, our results are compared in Figure 12 with the experimental measurements of Tritton [14], and numerical simulations of He and Doolen [23] performed with LBM. In this case our results fall about 5% below the literature data. This is mainly due to different boundary conditions and blockage ratios used in the various studies. In reference [23] lateral periodic boundaries and a constant inflow velocity profile instead of no-slip boundary conditions with a parabolic inflow velocity profile were used. Wagner [22] showed, using LBM, that $C_{\rm d}$ depends on the profile of the incoming flow and that $C_{\rm d}(\text{no-slip})/C_{\rm d}(\text{periodic}) = 0.82$ for $B = 0.1$. It seems natural to assume that a similar behavior holds also in the present case. Indeed, the comparison of our result $C_{\rm d}$(no-slip) with the result $C_{\rm d}$(periodic) obtained with LBM in reference [22] gives $C_{\rm d}(\text{no-slip})/C_{\rm d}(\text{periodic}) = 0.77$ at $Re = 48$ and $B = 0.125$, in good agreement with the value at $B = 0.1$.

In the unsteady-flow regime we computed also the lift coefficient

$$C_{\rm l} = \frac{2F_y}{n_{\rm av} v_{\max}^2 D}\,, \tag{6}$$

where F_y is the force exerted on the cylinder in the y-direction. This quantity oscillates periodically as shown in Figure 13(a). The characteristic frequency f of the vortex shedding was determined by a spectral analysis of the time series $C_{\rm l}$. The power spectrum corresponding to the time series shown in Figure 13(a), is shown in Figure 13(b). The frequency was used to determine the Strouhal number

$$St = \frac{fD}{v_{\max}}\,. \tag{7}$$

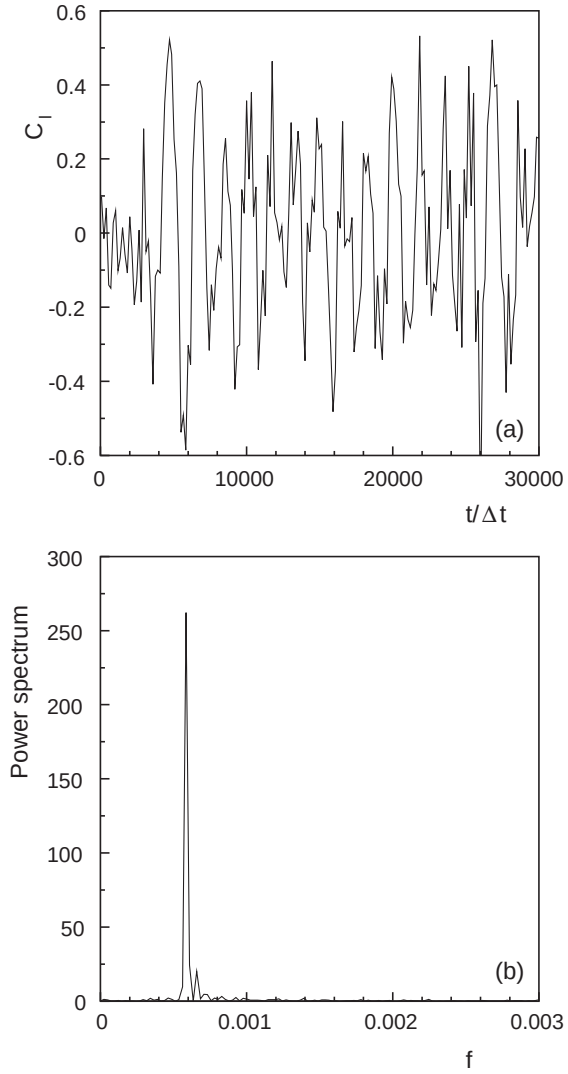

Fig. 13. (a) Time evolution of the lift coefficient for the square cylinder at $Re = 100$ and (b) the corresponding power spectrum.

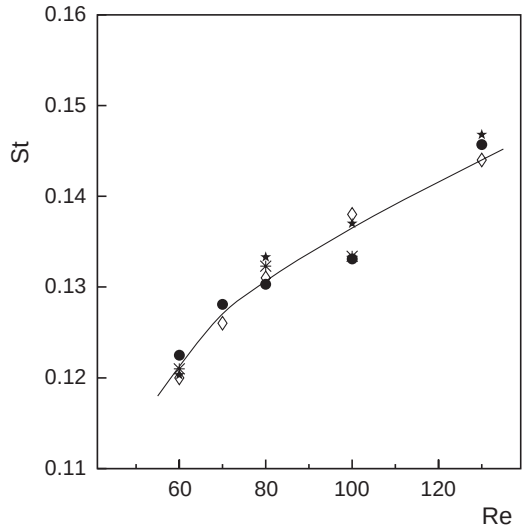

Fig. 14. The Strouhal number for the square cylinder as a function of the Reynolds number for different $v_{\max}$ values: this study with $v_{\max}\Delta t/a_0 = 0.2$ (•), 0.3 ($\star$), 0.36 ($*$); ($\diamond$) Breuer *et al.* [29]. The line is a guide to the eye.

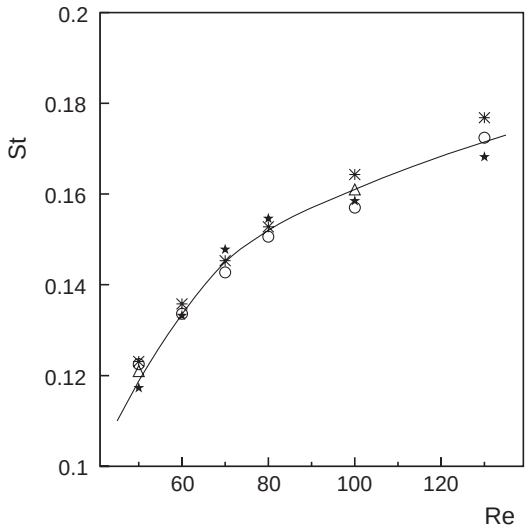

Fig. 15. The Strouhal number for the circular cylinder as a function of the Reynolds number: this study ($\star$) with $v_{\max}\Delta t/a_0 = 0.2$, ($\circ$) Tritton [14], ($\triangle$) He and Doolen [23], ($*$) Williamson [17]. The line is a guide to the eye.

Our data as a function of Re for different values of $v_{\max}$ are shown in Figure 14. It transpires that a better approximation to numerical data of Breuer *et al.* [29] is achieved for the lower value of $v_{\max}$. In the case of the circular cylinder (Fig. 15) our data lie within the range of scatter of the published data. It is worthwhile to stress that in this case the existing literature data were all obtained using different inflow conditions than in our study.

4 Conclusions

We have successfully applied multi-particle collision dynamics to simulate in two dimensions flow around a square and a circular cylinder for Reynolds numbers ranging from 10 to 130. The results are compared with previous experimental and numerical studies. The integral flow parameters, such as the recirculation length, the drag and lift coefficients, the Strouhal number, are found to be in agreement with existing literature data. The velocity profiles along and across the channel compare very well with previous simulations using different numerical techniques.

The present method includes thermal fluctuations which are not present in previous studies of this problem using lattice Boltzmann and finite-volume methods. This feature allows to define naturally the temperature. In equilibrium these fluctuations produce a logarithmic divergence of the viscosity with time [12,31]. Such a divergence is cut off by the finite size at long times. A thermal renormalization of the viscosity could indeed give account for the small deviations of the values for the recirculation

length and the drag coefficient compared to the lattice Boltzmann results.

The present model can find applications in several physical and chemical problems. It has been recently applied as a mesoscopic model of solvent dynamics in three dimensions [32], to study solvent dynamics coupled to a microscopic treatment of solute particles, such as colloids [33] and polymer chains [34,13] and to simulate binary [35] and ternary [36] fluid mixtures. In particular, the present results are relevant for studies of the interaction among large colloidal particles in solution.

We would like to thank D.M. Kroll and T. Ihle for many stimulating discussions, and U. Buchenau for kindly providing us with software for extracting data.

References

1. D.R. Noble, J.G. Georgiadis, R.O. Buckius, Int. J. Numer. Met. **23**, 1 (1996).
2. J. Bernsdorf, F. Durst, M. Schäfer, Int. J. Numer. Met. **29**, 251 (1999).
3. U. Frisch, B. Hasslacher, Y. Pomeau, Phys. Rev. Lett. **56**, 1505 (1986).
4. G.R. McNamara, G. Zanetti, Phys. Rev. Lett. **61**, 2332 (1988).
5. F.J. Higuera, J. Jimenez, Europhys. Lett. **9**, 663 (1989).
6. S. Succi, *The Lattice Boltzmann Equation* (Oxford University Press, Oxford, 2001).
7. P.J. Hoogerbrugge, J.M.V.A. Koelman, Europhys. Lett. **19**, 155 (1992).
8. I. Pagonabarraga, M.H. Hagen, D. Frenkel, Europhys. Lett. **42**, 377 (1998).
9. A. Malevanets, R. Kapral, J. Chem. Phys. **110**, 8605 (1999); **112**, 7260 (2000).
10. A. Lamura, G. Gompper, T. Ihle, D.M. Kroll, Europhys. Lett. **56**, 319 (2001).
11. G.A. Bird, *Molecular Gas Dynamics* (Clarendon Press, Oxford, 1976).
12. T. Ihle, D.M. Kroll, Phys. Rev. E **63**, 020201(R) (2001).
13. N. Kikuchi, A. Gent, J.M. Yeomans, Eur. Phys. J. E **9**, 63 (2002)
14. D.J. Tritton, J. Fluid Mech. **6**, 547 (1959).
15. M. Coutanceau, R. Bouard, J. Fluid Mech. **79**, 231 (1977); **79**, 257 (1977).
16. J.H. Gerrard, Philos. Trans. R. Soc. London, Ser. A **288**, 351 (1978).
17. C.H.K. Williamson, Phys. Fluids **31**, 2742 (1988).
18. M. Hammache, M. Gharib, Phys. Fluids A **1**, 1611 (1989).
19. R.W. Davis, E.F. Moore, L. P. Purtell, Phys. Fluids **27**, 46 (1984).
20. A. Okajima, J. Fluid Mech. **123**, 379 (1982).
21. F.J. Higuera, S. Succi, Europhys. Lett. **8**, 517 (1989).
22. L. Wagner, Phys. Rev. E **49**, 2115 (1994).
23. H. He, G. Doolen, J. Comput. Phys. **134**, 306 (1997); Phys. Rev. E **56**, 434 (1997).
24. F. Hayot, M. Raj Lakshmi, Physica D **40**, 415 (1989).
25. J.A.M.S. Duarte, U. Brosa, J. Stat. Phys. **59**, 501 (1990).
26. A. Vogeler, D.A. Wolf-Gladrow, J. Stat. Phys. **71**, 163 (1993).
27. A. Malevanets, R. Kapral, Europhys. Lett. **44**, 552 (1998).
28. J. Bernsdorf, T. Zeiser, G. Brenner, F. Durst, Int. J. Mod. Phys. C **9**, 1129 (1998).
29. M. Breuer, J. Bernsdorf, T. Zeiser, F. Durst, Int. J. Heat Fluid Flow **21**, 186 (2000).
30. C.H.K. Williamson, Annu. Rev. Fluid Mech. **23**, 477 (1996).
31. M.H. Ernst, E.H. Hauge, J.M.J. van Leeuwen, Phys. Rev. Lett. **25**, 1254 (1970).
32. E. Allahyarov, G. Gompper, Phys. Rev. E **66**, 036702 (2002).
33. S.H. Lee, R. Kapral, Physica A **298**, 56 (2001).
34. A. Malevanets, J.M. Yeomans, Europhys. Lett. **52**, 231 (2001).
35. Y. Hashimoto, Y. Chen, H. Ohashi, Comput. Phys. Commun. **129**, 56 (2000).
36. T. Sakai, Y. Chen, H. Ohashi, Phys. Rev. E **65**, 031503 (2002).